Journal of Colloid and Interface Science 614 (2022) 138–146

Contents lists available at ScienceDirect

Journal of Colloid and Interface Science

journal homepage: www.elsevier.com/locate/jcis

Homogeneous electric field and Li^+ flux regulation in three-dimensional nanofibrous composite framework for ultra-long-life lithium metal anode

Ai-Long Chen [a], Mingyu Gao [a], Lulu Mo [a], Jing Wang [c], Zhen Xu [d], Yue-E Miao [a,*], Tianxi Liu [a,b]

[a] State Key Laboratory for Modification of Chemical Fibers and Polymer Materials, College of Materials Science and Engineering, Donghua University, Shanghai 201620, P. R. China
[b] Key Laboratory of Synthetic and Biological Colloids, Ministry of Education, School of Chemical and Material Engineering, Jiangnan University, Wuxi, 214122, P. R. China
[c] Bristol Composites Institute (ACCIS), Department of Aerospace Engineering, Queen's Building, University of Bristol, University Walk, Bristol BS8 1TR, United Kingdom
[d] Department of Chemical Engineering, Imperial College London, London SW7 2AZ, United Kingdom

GRAPHICAL ABSTRACT

A zinc oxide-doped multichannel carbon nanofiber composite is facilely fabricated by electrospinning, which can homogenize both the electric field and ion flux distribution inside the lithium anode to suppress dendrites and achieve ultra-stable cycling performance.

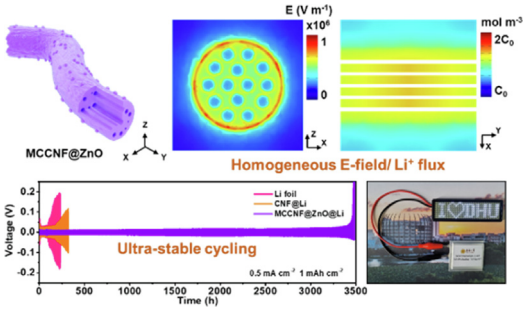

ARTICLE INFO

Article history:
Received 29 October 2021
Revised 12 January 2022
Accepted 13 January 2022
Available online 17 January 2022

Keywords:
Carbon nanofiber framework
Multi-channel structure
Homogenized electric field / Li^+ flux
Dendrite-free
Lithium metal anode

ABSTRACT

Lithium (Li) metal is considered as the best anode candidate for next-generation high-energy batteries due to its ultralow electrochemical potential and extremely high theoretical capacity. However, issues arising from the undesired growth of lithium dendrites and infinite volumetric change have seriously hindered the practical application of lithium metal batteries (LMBs). Here, we designed a super-lithiophilic amorphous zinc oxide-doped carbon nanofiber framework with uniformly-distributed and parallel multichannels (MCCNF@ZnO) to achieve the homogeneous distribution of electric field and Li^+ flux. By the assistances of *COMSOL* Multiphysics simulations and *ex-situ* scanning electron microscopy, we reveal that the Li metal preferentially deposits into the porous nanochannels inside the nanofibers, followed by its even distribution on the lithiophilic surface of MCCNF@ZnO. Furthermore, the conductive multichannels of the carbon nanofiber skeleton can effectively minimize the partial current density, thereby effectively avoiding the electrochemical polarization and assisting the uniform metallic deposition. As a result, MCCNF@ZnO exhibits a stable CE over 99.2% as the substrate after 500 cycles at the current density of 1 mA cm^{-2}. The symmetrical cell of lithium-loaded MCCNF@ZnO composite electrodes can

* Corresponding author.

https://doi.org/10.1016/j.jcis.2022.01.087

stably operate over 3300 h at 0.5 mA cm^{-2}, indicating the great potential of MCCNF@ZnO for stabilizing lithium metal anodes in practical applications of LMBs.

1. Introduction

Traditional lithium-ion batteries (LIBs) are approaching their energy-density upper limit due to the limited theoretical capacity of 372 mAh g^{-1} from inherent intercalation chemistries of graphite anodes, which can hardly meet the higher demand of battery systems with the explosive growth of portable electronic device and electric vehicles [1,2]. Beyond LIBs technologies, lithium (Li) metal is recognized as the most promising anode for high-energy Li metal batteries due to its high theoretical specific capacity (3860 mAh g^{-1}) and lowest electrode potential (−3.04 V vs standard hydrogen electrode) [3–5]. Despite the advantages of LMBs, its practical application has been seriously hindered by several issues, especially the notorious Li dendrite formation. The dendrites caused by the random plating/stripping process of metallic Li can increase the interface between the anode and electrolyte, which exacerbates the irreversible side reactions of the highly reactive metallic Li. Besides, the volume keeps expanding and contracting during the cycling process, leading to the pulverization of the anode. Consequently, the cycling stability and Coulombic efficiency (CE) of the metal anode constantly decrease as generated so-called "dead" Li. Additionally, Li dendrites can puncture the separator to directly contact the anode and cathode, leading to catastrophic safety hazards [6,7]. Several strategies have been focused on modification the Li/electrolyte interface to address these crucial issues [8–11], such as applying electrolyte additives or constructing a stable artificial solid electrolyte interface (SEI) on the Li metal anode to enhance its stability [12–16]. Although the performance can be improved up to a point by these approaches, the dendrites and large volume changes of anode still cannot be avoided during long-term cycling ascribed to the inhomogeneous nucleation and host-less instinct of Li metal [17–20].

Alternatively, constructing or modifying the current collectors has gained increasing attentions, because this approach can effectively minimize the local current density and thus largely diminish the dendritic Li. Moreover, the three-dimensional (3D) network skeleton can well adapt abundant Li to eliminate the volumetric fluctuation of the metallic anode during cycling [21–25]. Recently, considerable 3D porous frameworks, such as nickel foams and porous copper [26,27], carbon fiber skeletons have been conducted as eximious hosts for their large free space to accommodate Li [28–31]. However, these contributions only increase the battery life spans to some degree. The gradual formation of mossy and dendritic Li is still inevitable as Li exhibits poor wettability on the surface of these 3D skeletons. Consequently, "dead" Li still tends to form after preferentially detaching the Li dendrite roots off the skeleton surface [32]. Therefore, recent investigations targeting Li dendrite suppression in 3D porous skeletons have been mainly focused on the surface modifications by introducing lithiophilic materials such as elementary substances (Au, Ag and Si) [20,33,34], metal nitrides (TiN), and metal oxides (ZnO, MnO_2 and TiO_2) [35–38] to control the deposition of Li onto the skeletons. But limited by the delayed ion and electron transport in the substrates, it remains a key issue to guarantee the good rate performance and high CE upon long-term cycling [39–42]. The main reason is that there are severely uneven distributions of electric field (E-field) and ion concentration in different regions throughout the entire electrode [25,41,42]. Therefore, it is very imperative to develop highly conductive hosts with amounts of sub-space which are capable to effectively diminish the local current density and homogenize the E-field distribution and ion flux for ultra-stable and dendrite-free Li metal anodes.

Herein, a rationally designed super-lithiophilic amorphous zinc oxide-doped carbon nanofiber framework with uniformly distributed parallel nanochannels, denoted as MCCNF@ZnO, has been facilely prepared by electrospinning to replace the conventional 3D host for Li metal deposition. The highly interconnected parallel nanochannels effectively divide the hosting space into small confinements to accommodate electrolytes, which is beneficial to improving the ion migration rate and enhancing the electrolyte affinity of the substrate. Moreover, the uniformly dispersed amorphous ZnO with an excellent affinity toward Li helps the uniform Li nucleation as well. Consequently, the unique MCCNF@ZnO composite host can manipulate both the E-field and Li^+ flux distribution inside the electrode, which is beneficial to guild the uniform Li nucleation and plating behavior under various current densities. Therefore, the CE of MCCNF@ZnO anode stably maintains at 99.2% for 500 cycles at 1 mA cm^{-2} with the capacity of 1 mAh cm^{-2}. The MCCNF@ZnO@Li || LFP full cell paired with $LiFePO_4$ (LFP) cathode delivers excellent cycling stability, indicating the great potentials in couple with other cathode materials in LMBs.

2. Experimental section

2.1. Material Fabrication

The neat carbon nanofiber membrane (CNF) was fabricated by a facile electrospinning technique. First, 1.0 g of polyacrylonitrile (PAN, Macklin, M_w = 150000) was dissolved in 9 g of *N, N*-dimethylformamide (DMF, Shanghai Chemical Reagent Plant, 99.5%) with vigorous stirring at 25 °C for 12 h till become a homogeneous precursor solution. Then, a high-voltage of 12 kV was conducted to electrospin the precursor solution with an injection rate of 0.8 mL h^{-1}, while the distance between the spinneret and collector was fixed at 15 cm. Subsequently, the PAN membrane was peeled off from the aluminum foil and stablized for 1 h at 250 °C in air, followed by carbonized at 800 °C for 1 h in nitrogen (N_2, Air Shenzhong, Shanghai) atmosphere to obtain CNF.

The MCCNF@ZnO-3 membrane was obtained by a similar procedure with the precursor solution of 1.0 g of PAN, 0.2 g of polystyrene (PS, Aladdin (China), Mw = 35000), and 0.5 g of zinc acetate ($Zn(OAc)_2$, sinopharm chemical reagent Co., ltd) in 8.8 g of DMF under stirring at 60 °C for 6 h. Subsequently, the same pre-oxidized and carbonized processes were conducted to obtain the as-prepared nanofiber membrane. Finally, the MCCNF@ZnO composite was cut into the cycle disk with a diameter of 16 mm. For comparison, MCCNF@ZnO composites with different weight of $Zn(OAc)_2$ precursor at 0.1, 0.3, 0.7 g were also fabricated using the same procedures, which were denoted as MCCNF@ZnO-1, MCCNF@ZnO-2 and MCCNF@ZnO-4, respectively.

2.2. Characterizations

Morphology of the materials was observed with field emission scanning electron microscope (JSM-7500F) and transmission electron microscopy (TEM, Talos F200S). The Energy-dispersive X-ray spectroscopy (EDS) was conducted to obtain the elemental mapping. XRD spectra were processed with a Bruker-D8 ADVANCE X-

ray diffractometer. The nitrogen adsorption-desorption isotherms are obtained from the Quantachrome Autosorb-iQ/MP®XR system. The specific surface area was illustrated by Brunauer-Emmett-Teller analysis. Raman spectra were conducted at an excitation wavelength of 532 nm with Renishaw (inVia reflex). XPS measurements were performed on an X-ray photoelectron spectrometer (XPS, Physical Electronics PHI5802) with a monochromatic Al K_α X-Ray source. A TG 209 F1 Libra thermogravimetric analyzer was carried out at a rate of 20 °C min^{-1} under the airflow to obtain the thermogravimetric analysis (TGA) of samples.

2.3. Electrochemical measurements

CR 2025 coin cells were assembled in an Ar-filled gloved glove box. The electrochemical performance was evaluated by A Land 2001A battery testing system. Li metal (China Energy Lithium Co., Ltd) was coupled with Cu foil, CNF and MCCNF@ZnO current collectors to measure the Coulombic efficiency (CE). A fixed amount (40 μL) of 1 M lithium bis(trifluoromethane sulfonyl) imide (LiTFSI, DoDoChem, 99.8%) in 1, 3-dioxolane (DOL, DoDoChem, 99.95%) and 1, 2-dimethoxyethane (DME, DoDoChem, 99.95%) (volume ratio: 1:1) with 1% $LiNO_3$ (DoDoChem, 99.9%) was used as the electrolyte. Besides, 1.0 M lithium hexafluorophosphate ($LiPF_6$) dissolved in a mixed solvent of ethylene carbonate (EC) and diethyl carbonate (DEC) without any additive (1.0 M $LiPF_6$ /EC:DEC = 1:1 by vol) was adopted to investigate the performance of MCCNF@ZnO@Li in the carbonate-based electrolyte. A Celgard 2400 membrane was used as the separator. The cut-off voltage of stripping process was fixed at 1 V (vs Li^+/Li) after plating a certain amount of Li. Electrochemical impedance spectra (EIS) measurements were conducted via the CHI660E electrochemical workstation in the frequency range of 10 mHz to 100 kHz.

Symmetrical cells were fabricated by pre-depositing 3 mAh cm^{-2} of Li on the various current collector at 1 mA cm^{-2} and the cells were disassembled to extract the pre-plating electrode. Then, symmetric cells were assembled into coin cells. Full cells were assembled with $LiFePO_4$ as cathode and Li foil, CNF@Li or MCCNF@ZnO@Li as the anodes, respectively. The electrolyte and separator were the same as that in the half cells. The $LiFePO_4$ cathode was prepared by mixing $LiFePO_4$ (Canrd New Energy Technology, Guangdong), super-P (Canrd) and polyvinylidene difluoride (PVDF) (Arkema) in *N*-methyl-*2*-pyrrolidone (NMP, Shanghai Lingfeng Chemical, 99.5%) at a mass ratio of 8:1:1. The slurry was coated onto an aluminum foil (Canrd) followed by drying in a vacuum with an average areal loading of 5.0 mg cm^{-2}. The cells were cycled between 2.4 and 4.2 V during the cycling and rate tests. The soft-packed MCCNF@ZnO || LFP batteries were assembled in an Ar-filled gloved glove box with Celgard 2400 as a separator, while the LFP cathode with the average mass loading of ca. 5 mg cm^{-2} and cut into a square with around 18.0 cm^2 area (4.5 cm ∗ 4.0 cm).

2.4. Numerical simulation

In order to demonstrate the E-field and Li^+ distributions during the process of lithium deposition, the single fiber has been extracted and cut open to compare the distinction between the solid CNF and multichannel MCCNF@ZnO fibers by COMSOL Multiphysics 5.6.0.280 software. At the simulation process, the CNF and MCCNF@ZnO fibers were cut along the X-Z plane to illustrate the E-field distribution within the fibers, while both fibers were cut open along the X-Y plane at the middle of fibers to observe the Li^+ flux distribution. In the above two simulations, the Li^+ diffusion coefficient was set to 1.5×10^{-10} m^2 s^{-1} and the initial electrolyte concentration (C_1) was set as 1000 mol m^{-3} (1 mol L^{-1}).

3. Results and discussion

The finite element simulation results based on COMSOL Multiphysics in Fig. 1 demonstrate the advantages of MCCNF@ZnO in manipulating the uniform distributions of both E-field and Li^+ flux compared to solid carbon nanofibers (CNF). By taking a single fiber of MCCNF@ZnO (Fig. 1a) and CNF (Fig. 1b) as the model, a more uniform E-field distribution within the multi-channels of MCCNF@ZnO is observed (Fig. 1c) compared to the severe E-field polarization surrounding the surface of the solid CNF (Fig. 1d). The corresponding cross-sectional E-field profiles along the normal Z direction of the single fiber also imply a smaller electric field intensity differential within the multi-channels of MCCNF@ZnO (Fig. 1e), which is beneficial to homogenous lithium deposition. In consideration of the more dominant role of Li^+ concentration in the mid to late Li deposition period, Li^+ flux distributions within MCCNF@ZnO and CNF are further obtained. MCCNF@ZnO presents more homogeneously distributed Li^+ flux within its multi-channels without any 'hot spots' (Fig. 1f), while the Li^+ flux approaching the surface of CNF keeps at a high concentration which may cause the accumulation of Li dendrites (Fig. 1g). Besides, the corresponding Li^+ flux concentration along the X-Y cross-sectional plane in the middle of the fiber indicates higher uniformity within the MCCNF@ZnO. And the concentration inside the channels is higher than the fiber surface (Fig. 1h), which is beneficial for the uniform deposition of Li without any dendrites.

The super-lithiophilic MCCNF@ZnO composite nanofiber host is rationally fabricated via a simple electrospinning route as illustrated in Fig. 2a. Briefly, a homogeneous precursor solution containing polystyrene (PS), polyacrylonitrile (PAN) and $Zn(OAc)_2$ is electrospun into the polymer composite nanofiber membrane. Subsequently stabilization in air and then carbonization at 800 °C in N_2, super-lithiophilic amorphous ZnO are uniformly distributed on the 3D CNF skeleton with multi-porous nanochannels (Fig. 2b,c). The MCCNF@ZnO composite nanofibers show a well-interconnected network structure with a fiber diameter ranging 800–1000 nm. Meanwhile, the corresponding energy-dispersive X-ray spectroscopy (EDS) mapping images (Fig. S1) indicates that elemental carbon (C), zinc (Zn) and oxygen (O) are all uniformly distributed in MCCNF. To optimize the loading amount of ZnO, MCCNF@ZnO composites are also prepared from precursors containing different weight ratios of $Zn(OAc)_2$, which are denoted as MCCNF@ZnO-1, MCCNF@ZnO-2, MCCNF@ZnO-3 and MCCNF@ZnO-4 (Fig. S2), respectively. As shown in Fig. S3, evenly distributed nano-bumps appear on the surface of MCCNF@ZnO fibers as the content of ZnO increases. Besides, the pore size of the parallel nanochannels within MCCNF@ZnO composites gradually increases from 20 to 75 nm, which can create increasing free spaces for uniform distribution of Li^+ flux. However, when the Zn $(OAc)_2$ content increases to a certain value, the spinnability of the composite precursor solution decreases with a large number of spindles appearing in the MCCNF@ZnO-4 composite fibers. Hence, MCCNF@ZnO-3 is chosen as the optimized sample in the following statement if without any special instructions. To further observe the microscopic structure of MCCNF@ZnO composites, transmission electron microscopy (TEM) images are displayed in Fig. 2d. Paralleled nanochannels with the uniform distribution of C, Zn, and O elements are clearly observed within the nanofibers (Fig. 2e), which are expected to homogenize the Li^+ concentration for uniform and smooth Li deposition. The high-resolution TEM images further reveal an amorphous structure without any lattice fringes in the MCCNF@ZnO composite (Fig. S4), which is in consistent with the X-ray diffraction patterns (XRD) in Fig. S5.

The detailed compositions of MCCNF@ZnO are shown in the Raman spectra (Fig. 2f), which presents a peak localized at

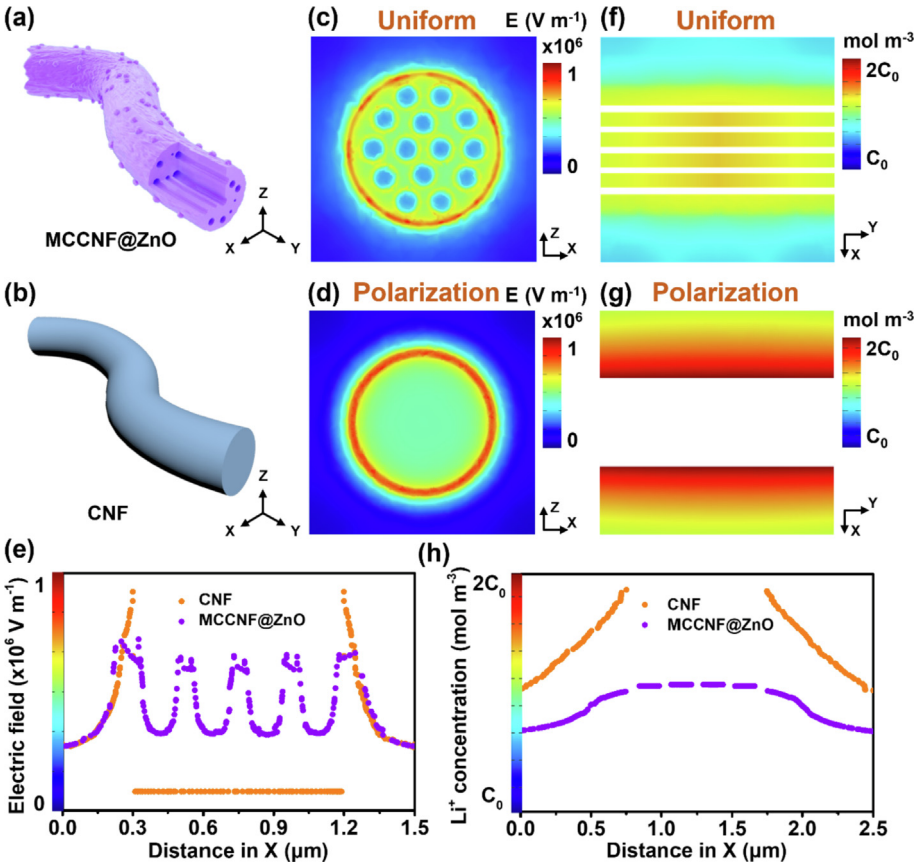

Fig. 1. Simulation models of the domains of (a) MCCNF@ZnO and (b) CNF. The corresponding E-field distributions of (c) MCCNF@ZnO and (d) CNF. Simulation of Li^+ flux distribution within (f) MCCNF@ZnO and (g) CNF. (e) E-field profiles along the X direction of the X-Z plane upon CNF and MCCNF@ZnO electrodes. (h) Li^+ distribution along the X-axis within the X-Y plane of CNF and MCCNF@ZnO. The background color indicates the intensity of E-field or the Li^+ concentration, while the white region represents the solid inner-body of the fiber.

437 cm^{-1} assigned to the non-polar optical phonon E2 (high) mode of ZnO [43]. The typical D-peak (~1350 cm^{-1}) and G-peak (~1580 cm^{-1}) of disordered carbons can be observed in both MCCNF@ZnO and CNF. Meanwhile, X-ray photoelectron spectroscopy (XPS) further verify the ZnO incorporation (Fig. S6). The peaks at 531.3, 532.5, and 534.6 eV are assigned to the O^{2-} in ZnO [44,45], –OH and –COOH groups in MCCNF@ZnO composite in the high-resolution O1s scan (Fig. S6b) [46,47], respectively. The two symmetric peaks centered at 1022.7 and 1045.8 eV in the high-resolution Zn 2p spectrum (Fig. S6c) are corresponding to Zn $2p_{3/2}$ and Zn $2p_{1/2}$, respectively. The binding energy and calculated splitting width (23.1 eV) well indicate the presence of Zn^{2+} and formation of ZnO within the MCCNF@ZnO composite [48,49]. The multichannel property of MCCNF@ZnO is further investigated by Brunauer-Emmett-Teller (BET) analysis (Fig. 2g). A noticeable high BET surface area of 643.137 m^2 g^{-1} is achieved for MCCNF@ZnO and the pore size is dominated at 10 ~ 80 nm (the inset in Fig. 2g) to effectively increase the contact area between the lithiophilic matrix and Li^+, being beneficial for reducing the exchange current density to eliminate the "hot spots".

In order to investigate the influence of ZnO content on the electrochemical performance, asymmetric batteries are assembled by directly using the MCCNF@ZnO composites as the current collectors against the metallic lithium. As the ZnO content increases, the nucleation overpotential gradually decreases (Fig. 3a,b), which can be ascribed to the superior lithiophilicity of ZnO and large deposition area of MCCNF@ZnO. Fig. 3c and S7 presents a small electrolyte contact angle of nearly 0° for MCCNF@ZnO while Cu and CNF show higher contact angles of 26.8° and 12.4°, respectively, further indicating the high affinity between the electrolyte and MCCNF@ZnO with multi-channels. However, the overloading of ZnO would deteriorate the uniform structure and specific surface area of MCCNF@ZnO, which conversely increases the nucleation overpotential. To tentatively investigate the plating morphology of lithium metal on the MCCNF@ZnO composite hosts and traditional copper foil, 5 mAh cm^{-2} of Li metal was deposited by a current density of 1 mA cm^{-2}. As shown in Fig. S8, bulk dendrites appear on the copper foil surface due to its poor lithiophilicity and uneven current density distribution. As a comparison, much smoother lithium deposition morphologies are observed on the surface of all MCCNF@ZnO composites, although some uneven deposition appears after a high loading amount of ZnO in MCCNF@ZnO-4. The voltage profiles of first-cycle at 1 mA cm^{-2} also demonstrate the superiority of MCCNF@ZnO on lithium plating behavior. As shown in Fig. S9, the MCCNF@ZnO composite exhibits an ultralow nucleation overpotential of 11.7 mV ascribed to the reasonable design of MCCNF@ZnO composite with multi nanochannels and super-lithophilic ZnO to facilitate Li^+ transfer, and highly conductive network with ultrahigh surface area to homogenize the E-filed. In contrast, CNF and copper foil deliver higher overpotentials of 36.2 and 66.3 mV, respectively.

The cycling stability is further evaluated by CE, which is defined as the ratio between the capacity of stripping to plating during charge/discharge processes, in asymmetrical cells by employing Li foil as the lithium source and Cu, CNF and MCCNF@ZnO composite hosts as working electrodes, respectively. Obviously, the CE of MCCNF@ZnO is stabilized at 99.2% for over 500 cycles at 1 mA cm^{-2} for 1 mAh cm^{-2} (Fig. 3d), suggesting the faster Li^+ migration kinet-

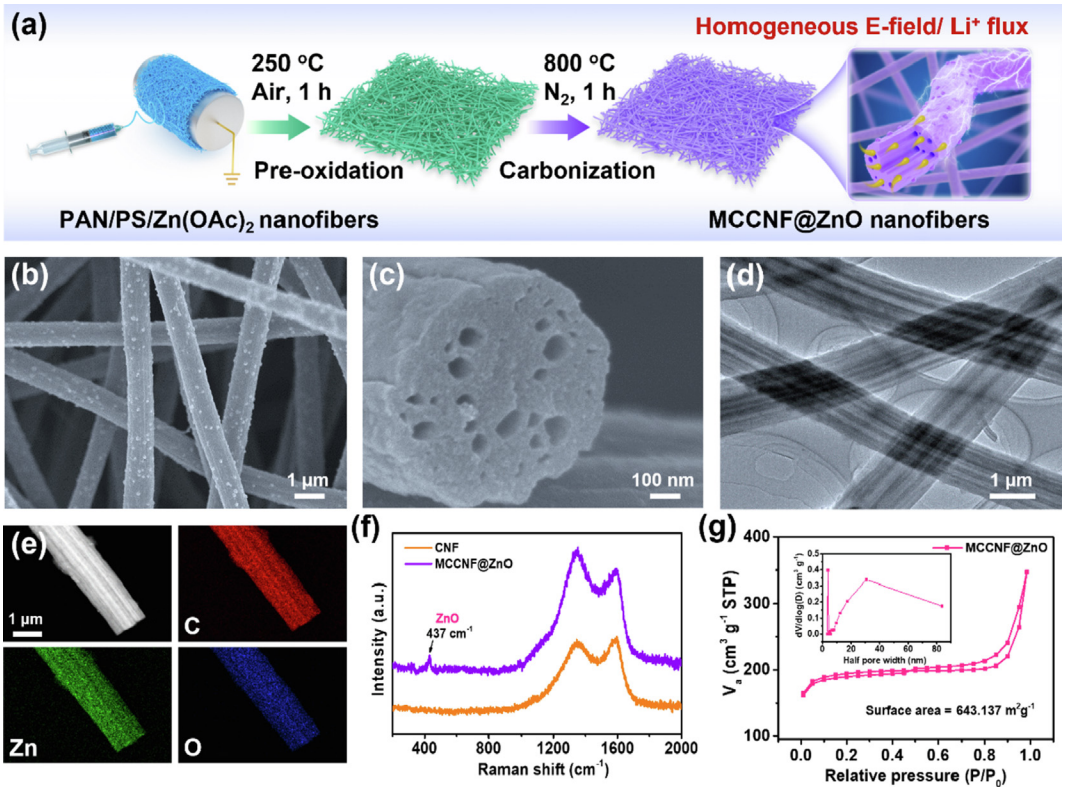

Fig. 2. (a) Schematic illustration showing the synthesis procedure of MCCNF@ZnO. SEM images of MCCNF@ZnO: (b) top-view and (c) cross-section view. (d) TEM image and (e) the corresponding elemental mappings of C, Zn, O. (f) Raman spectra of MCCNF@ZnO. (g) N_2 adsorption and desorption isotherms of MCCNF@ZnO. The inset shows the corresponding pore size distributions.

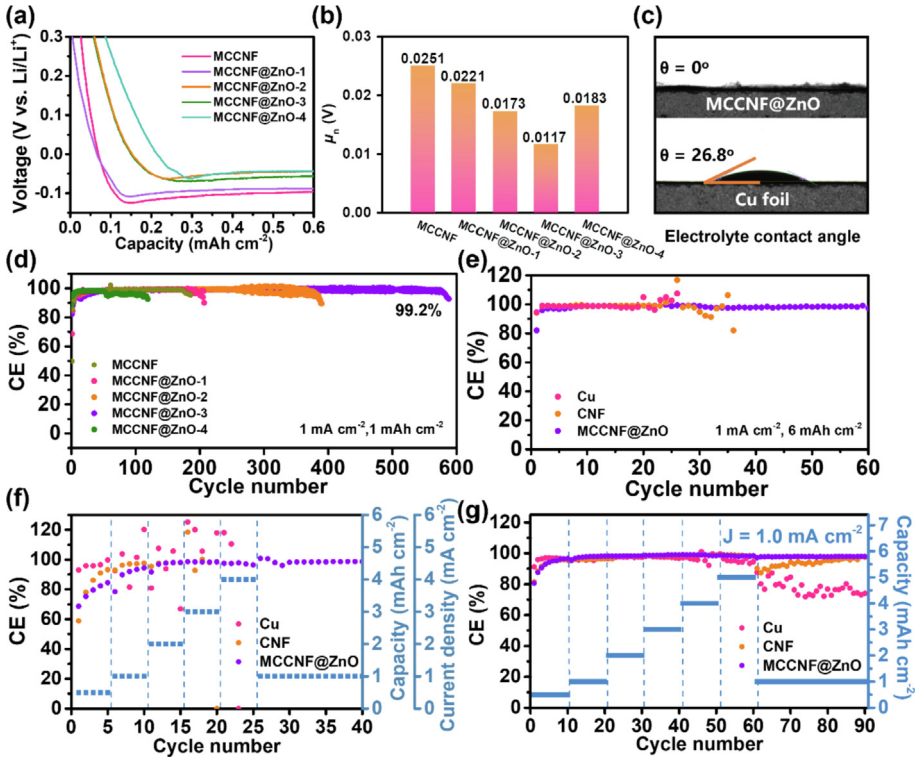

Fig. 3. (a) Voltage profiles for the first-cycle discharge profiles of MCCNF@ZnO current collectors at 1.0 mA cm^{-2} with 1.0 mAh cm^{-2}, and (b) the corresponding nucleation overpotential histogram and (d) CE. (c) Contact angles of LiTFSI-DOL/DME electrolyte on MCCNF@ZnO and Cu foil. (e) CE of Cu, CNF and MCCNF@ZnO current collectors at 1 mA cm^{-2} and 6 mAh cm^{-2}. (f) CE of Cu, CNF and MCCNF@ZnO current collectors with increasing current density and capacity from 0.5 mA cm^{-2}, 0.5 mAh cm^{-2} to 4 mA cm^{-2}, 4 mAh cm^{-2}, and (g) the corresponding CE with increasing capacity from 0.5 to 5 mAh cm^{-2} at 1 mA cm^{-2}.

ics and more stable interfacial properties without side reactions. In contrast, the CE of Cu foil rapidly decreases to below 80.0% with large fluctuation after only 70 cycles due to the uneven nucleation of Li^+ and the formation of Li dendrites (Fig. S10a). When cycled at the high current density of 2 and 3 mA cm^{-2}, the CE of MCCNF@ZnO remains at 97.5% after 130 cycles (Fig. S10b) and 96.2% after 120 cycles (Fig. S10c), indicating a much durable lifespan than those of Cu foil and CNF electrodes. Notably, even at the high capacity of 6 mAh cm^{-2}, the CE of the MCCNF@ZnO electrode still keeps as high as 98.2% with an impressively long lifespan (Fig. 3e). From the specific capacity voltage curves for the first two cycles of MCCNF@ZnO, it can be indicated that 0.15 mAh cm^{-2} of Li metal participated in the lithiation of ZnO, and 0.02 mAh cm^{-2} participated in the formation of a stable SEI (Fig. S11). The CE under increasing current densities and areal capacities are also conducted to investigate the rate superiority of various electrodes (Fig. 3f,g). The copper foil suffers from a large fluctuation at the current density of 1 mA cm^{-2} or the capacity of 3 mAh cm^{-2}, while the CNF fails only at the current density of 2 mA cm^{-2} or the capacity of 4 mAh cm^{-2}. Nonetheless, the MCCNF@ZnO electrode with multi porous channels delivers excellent CE even at gradually increased current densities up to 4 mA cm^{-2} and areal capacities over 5 mAh cm^{-2}, indicating its outstanding rate performance and higher capacity for potential practical applications.

To better understand the electrochemical plating/stripping mechanisms of metallic Li into both CNF and MCCNF@ZnO electrodes, Li plating is carried out under various capacities from 1 to 6 mAh cm^{-2} at 1 mA cm^{-2} (Fig. 4a). According to *COMSOL* simulation upon the Li^+ flux within MCCNF@ZnO, the ion concentration inside the multi porous channels is higher than the fiber surface (Fig. 1h). In consequence, Li metal prefers to be deposited within the multi-channels of MCCNF@ZnO electrode (Fig. 4b), which is further investigated by the *ex-situ* SEM observations in Fig. 4c-f. At 1.0 mAh cm^{-2}, no Li deposition can be observed on the outside of MCCNF@ZnO. This can be attributed to that the plated lithium mainly participates in the lithiation of ZnO to form LiZn alloy, while the remaining part is plated into the hollow nanochannels with amount sub-space as shown in Fig. 4c. With the increasing plating capacity from 2.0 to 3.0 mAh cm^{-2}, the multi-channels of MCCNF@ZnO fibers are gradually filled with more Li metal (Fig. 4d), but the outside of the fibers remains smooth without any deposition (Fig. 4e). When further plating to 4.0 mAh cm^{-2}, lithium metal starts to be uniformly coated along the surface of MCCNF@ZnO fibers as the channels are completely filled (Fig. 4f). As illustrated in Fig. 4g,h, the surface of MCCNF@ZnO fibers maintains smooth with metallic luster due to the uniform coating of a thin lithium layer after deposition to 4.0 mAh cm^{-2}. Upon further plating to 5.0 and 6.0 mAh cm^{-2}, Li is densely deposited surround-

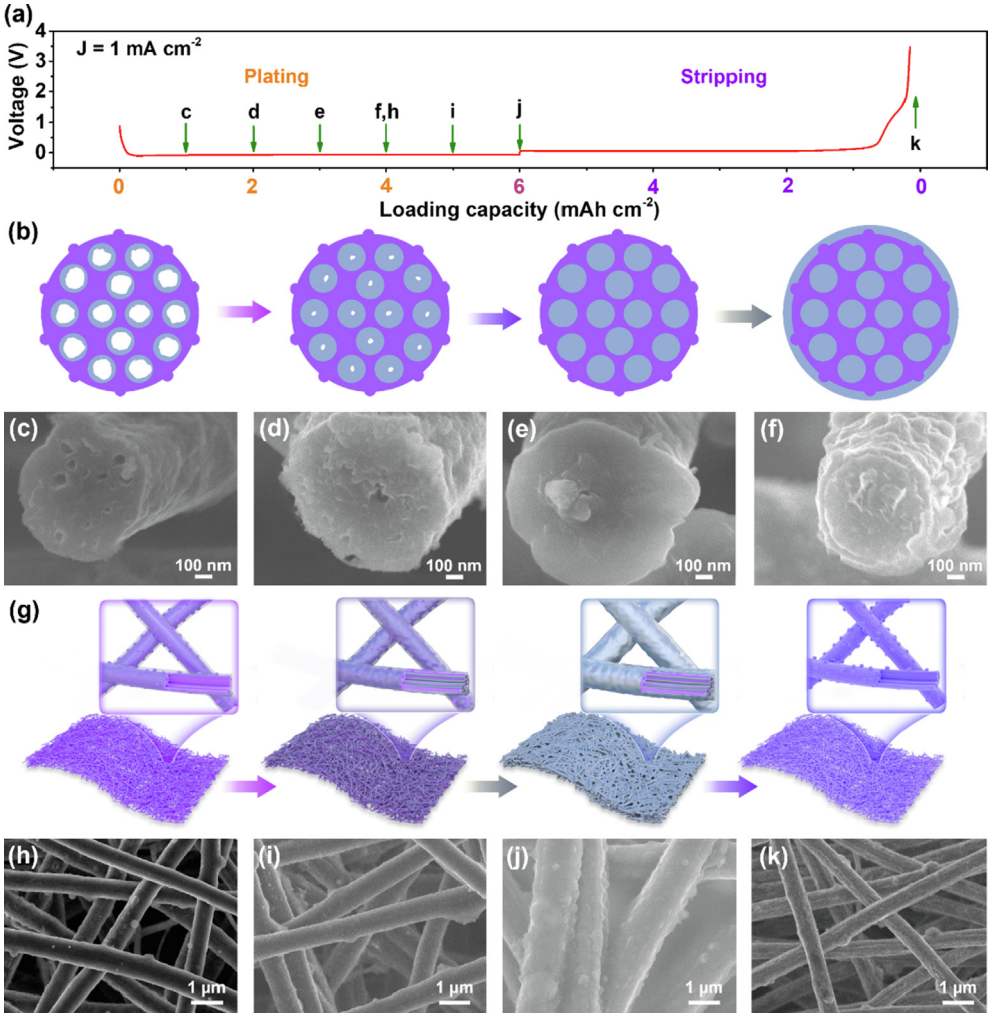

Fig. 4. Morphology evolution of the MCCNF@ZnO electrode during Li stripping and plating. (a) The votage profile of first-cycle plating/stripping in MCCNF@ZnO at 1 mA cm^{-2}. (b) Schematic diagram of Li plating process for MCCNF@ZnO before 4.0 mAh cm^{-2} and (g) up to 6.0 mAh cm^{-2}. SEM images of MCCNF@ZnO after depositing capacities at (c) 1.0, (d) 2.0, (e) 3.0, (f), (h) 4.0, (i) 5.0, and (j) 6.0 mAh cm^{-2}. (k) SEM image of MCCNF@ZnO after stripping of 6.0 mAh cm^{-2}Li.

ing all the MCCNF@ZnO fibers in the whole membrane (Fig. 4i,j), which is guided by the uniform distribution of Li^+ flux as demonstrated by the *COMSOL* simulation (Fig. 1f). Besides, a clean fiber surface without any residuals recovers after the Li stripping process (Fig. 4k), further indicating the highly stable and reversible Li plating/stripping process of MCCNF@ZnO. Consequently, the uniform deposition behavior of Li metal would regulate the subsequent growth of lithium along with the fibers. The excellent reversibility during the Li stripping process is enabled by the integrated and compact flexible matrix of MCCNF@ZnO extinguishing the "dead" Li. This is very different from the deposition behavior on the CNF electrode (Fig. S12a), with obvious large Li aggregates and dendrites formed at the junctions of interconnected CNF fibers after plating at 1.0 mAh cm^{-2} of Li in Fig. S12b. With further plating, Li metal appears in a large chunk-shape which is almost shedding off from the surface of CNF (Fig. S12c,d). Furthermore, the petal-shaped "dead" Li remains at the junctions of CNF membrane after striping at 3.0 mAh cm^{-2} (Fig. S12e), which means lower CE to accelerate the Li dendrite growth and deteriorated cycling stability.

The symmetrical cell is also conducted to evaluate the long-term plating/striping performance of MCCNF@ZnO@Li as a free-standing Li metal composite anode. Fig. 5a presents the cycling properties of various symmetric cells at 0.5 mA cm^{-2} for 1.0 mAh cm^{-2}. Remarkably, the symmetric cell with MCCNF@ZnO@Li composite anode exhibits a consistent overpotential of 10 mV and an outstanding cycling stability approaching 3500 h. By contrast, the cells with both CNF@Li and Li foil show large overpotentials, failing after 230 and 320 h, respectively. The voltage hysteresis means the voltage difference between the process of charge and discharge, which can directly exhibit the voltage variation during redox cycling. The MCCNF@ZnO@Li anode maintains a stable voltage hysteresis below 20 mV after 800 cycles in Fig. S13, suggesting the excellent kinetic performance and uniform deposition of Li. However, the CNF@Li and Li anodes show larger voltage variations with fluctuations during cycling. When the current density increases to 1 mA cm^{-2}, the Li foil and CNF@Li symmetric cells display gradually increased voltage overpotentials and obvious failures after 140 and 230 h (Fig. S14), respectively. More impressively, the MCCNF@ZnO@Li anode exhibits remarkable cycle stability with a constant overpotential of 20 mV during the cycling of 1000 h. The current density conducted from 0.5 to 6 mA cm^{-2} further demonstrates that the cells with Li foil and CNF@Li show unstable cycling with large voltage hysteresis even at low current densities (Fig. 5b). In contrast, the MCCNF@ZnO@Li cell exhibits eminent cycling with low voltage overpotentials of 11.8, 22.6, 31.9, 45.9 and 58.3 mV at 0.5, 1, 2, 4 and 6 mA cm^{-2}, respectively, indicating favorable Li plating/stripping kinetics and superior interfacial properties. A constant high current of 5 mA cm^{-2} is also conducted to continuous deposit the Li metal in the various anodes. It is obvious that the Sand's time of MCCNF@ZnO@Li is eight times longer than that of CNF@Li (Fig. S15), thus effectively reducing the "tip effect" in MCCNF@ZnO@Li to achieve a uniform and dendrite-free lithium deposition. The high-resolution XPS spectra were further collected on the surface and inner layer of MCCNF@ZnO@Li anode after cycling. The C 1s and F 1s spectra on the surface of MCCNF@ZnO@Li after cycling exhibit some typical peaks of the SEI layer (Fig. S16a, b), which are assigned to the decomposition products of organic solvents [50–52]. Obviously, these peaks are decreased or disappeared after etching in the Li 1s spectra. Compared with the spectra before etching, two new peaks of Li^0 and Li-Zn were detached in Li 1s (Fig. S16c). The new peaks appearing at lower binding energies of 1021.7 eV and 1045.2 eV for Zn $2p_{3/2}$ and Zn $2p_{1/2}$ (Fig. S16d), compared to those (1022.7 and 1045.8 eV) of the pristine ZnO (Fig. S6c), indicate the formation of the Li_xZn alloy. [53,54]. Electrochemical impedance spectroscopy (EIS) is con-

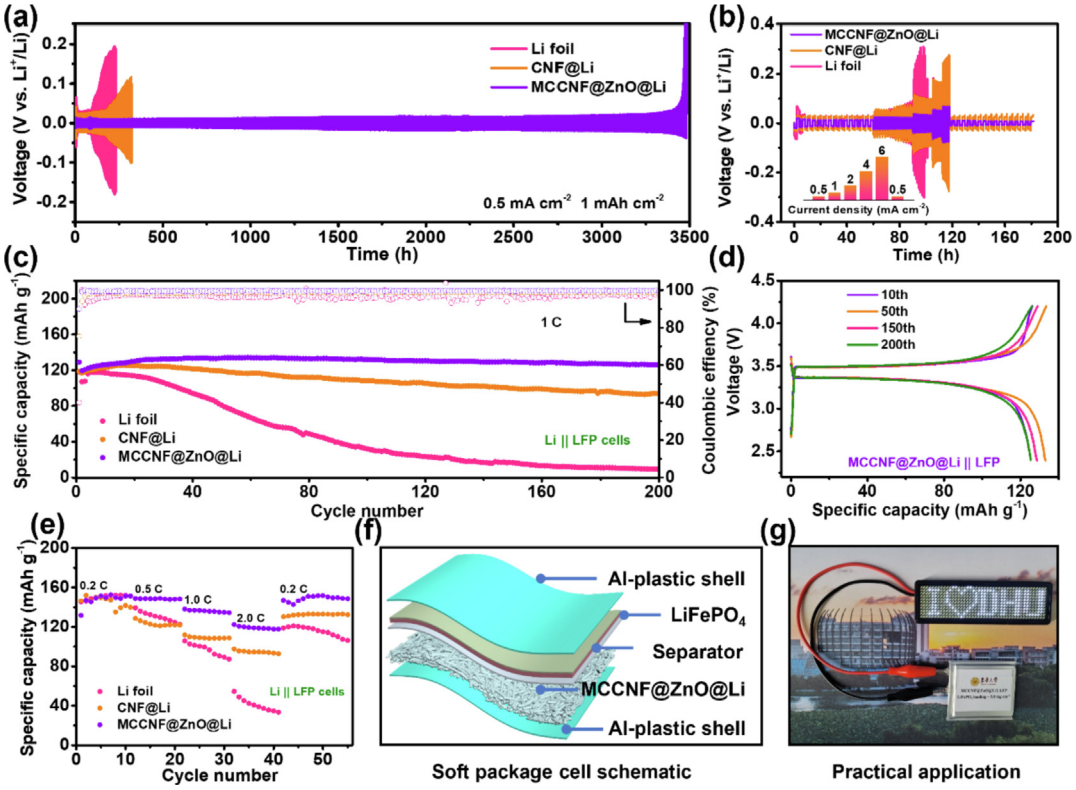

Fig. 5. (a) Voltage profiles and of symmetric Li foil, CNF@Li and MCCNF@ZnO@Li cells at the galvanostatic current density of 0.5 mA cm^{-2} and (b) increasing current densities. (c) Cycling performance of the full cells with different anodes coupled with $LiFePO_4$ cathode, and (d) the corresponding charge-discharge profiles of MCCNF@ZnO@Li anode after various cycles at the rate of 1.0C. (e) The rate capabilities of the full cells with three types of anodes. (f) The schematic of MCCNF@ZnO@Li || LFP soft-package cell. (g) The optical photograph of lighting up a Panel LED by the MCCNF@ZnO@Li || LFP soft-package cell.

ducted to further investigate the stability of interface during redox cycling in Fig. S17a,b. The charge-transfer resistance (R_{ct}) values of MCCNF@ZnO@Li are much smaller than those of CNF@Li in Fig. S17c, demonstrating the much faster kinetics benefitting from the uniformly dispersed super-lithiophilic amorphous ZnO and multi-channels within the whole nanofibrous anode.

To explore the superiority of MCCNF@ZnO@Li in practical applications, the LFP cathode is coupled with Li foil, CNF@Li and MCCNF@ZnO@Li anodes to assemble full cells. Before the test, all composite anodes are pre-plated with 3.0 mAh cm^{-2} of Li at 1.0 mA cm^{-2}. The cycle stability in Fig. 5c,d indicate that the MCCNF@ZnO@Li || LFP full cell achieves a very stable cycling for 200 cycles with a CE of 99.5%. In contrast, the capacity of the CNF@Li || LFP cell gradually decays to 85 mAh g^{-1} only after 200 cycles (Fig. S18a), indicating serious Li loss during cycling. Furthermore, the capacity of Li || LFP cell rapidly decays after 50 cycles (Fig. S18b), which is mainly caused by the lossy Li deposition at the "hot spots" that accelerates the dendritic Li growth and consumption of electrolyte. The rate performance of the full cells is also tested in Fig. 5e, with the corresponding voltage profiles presented in Fig. S19. It is clear that the MCCNF@ZnO@Li || LFP cell delivers superior rate performance over those of CNF@Li || LFP and Li || LFP systems, especially at higher rates. The cell based on the MCCNF@ZnO@Li anode can also achieve an excellent cycling performance over 200 cycles when cycling at 0.5 C (Fig. S20), which can be attributed to the uniform deposition of Li metal into the rationally designed multichannel network with an amount of super-lithiophilic groups. In addition, the MCCNF@ZnO@Li anode could run stably in carbonate-based electrolytes (Fig. S21). Therefore, this work confirms the feasible design of MCCNF@ZnO@Li anode for high-energy Li metal batteries in practical applications. On this basis, the MCCNF@ZnO@Li is assembled in a soft-package battery to confirm its practical application in real life in Fig. 5f. The soft-package battery with MCCNF@ZnO@Li anode and LFP cathode is able to light a LED panel with a specific pattern of 506 white bulbs (Fig. 5g), indicating the great potential in practical applications.

4. Conclusions

In this work, we have designed a super-lithiophilic MCCNF@ZnO fibrous composite with uniformly distributed multi-parallel nanochannels as a Li metal anode host to homogenize both the E-field and Li^+ flux distributions. The MCCNF@ZnO composite skeleton provides massive super-lithiophilic nucleation sites with lower overpotential and stronger binding affinity for the ultra-uniform and stable plating/stripping of Li metal, thus effectively avoiding "dead" Li and improving the stability over the entire operating process. As a result, the MCCNF@ZnO composite host exhibits an eminent cycling stability with a high CE of 99.2% after 500 cycles at 1.0 mA cm^{-2} and a small voltage potential of 12 mV over a long-lifespan of 3300 h at 0.5 mA cm^{-2}. Benefiting from the highly reversible redox cycling process and fast charge kinetics, the MCCNF@ZnO@Li || LFP full cell delivers an extraordinarily long lifetime. We believe that this work can provide the design guidance of stabilizing Li metal anodes, which is of great significance for the practical implementation of next-generation lithium metal batteries with high-energy denstiy, like Li-S and Li-air systems.

CRediT authorship contribution statement

Ai-Long Chen: Conceptualization, Data curation, Formal analysis, Investigation, Methodology, Visualization, Writing – original draft, Writing – review & editing. **Mingyu Gao:** Investigation. **Lulu Mo:** Investigation. **Jing Wang:** Investigation. **Zhen Xu:** Investigation. **Yue-E Miao:** Funding acquisition, Supervision, Writing – review & editing. **Tianxi Liu:** Funding acquisition, Supervision, Writing – review & editing.

Declaration of Competing Interest

The authors declare that they have no known competing financial interests or personal relationships that could have appeared to influence the work reported in this paper.

Acknowledgments

The authors are grateful for the financial support from the National Natural Science Foundation of China (22075042), Natural Science Foundation of Shanghai (20ZR1401400), the Fundamental Research Funds for the Central Universities and DHU Distinguished Young Professor Program (LZB2021002).

Appendix A. Supplementary material

Supplementary data to this article can be found online at https://doi.org/10.1016/j.jcis.2022.01.087.

References

[1] J.B. Goodenough, K.-S. Park, The Li-ion rechargeable battery: a perspective, J. Am. Chem. Soc. 135 (4) (2013) 1167–1176.
[2] Z.W. Seh, Y. Sun, Q. Zhang, Y.i. Cui, Designing high-energy lithium–sulfur batteries, Chem. Soc. Rev. 45 (20) (2016) 5605–5634.
[3] G. Liang, J. Wu, X. Qin, M. Liu, Q. Li, Y.-B. He, J.-K. Kim, B. Li, F. Kang, Ultrafine TiO_2 decorated carbon nanofibers as multifunctional interlayer for high-performance lithium–sulfur battery, ACS Appl. Mater. Interfaces 8 (35) (2016) 23105–23113.
[4] J. Yang, T. Feng, C. Zhi, J. Li, H. Zhou, C. Chen, Y. Song, M. Wu, Bimetallic composite induced ultra-stable solid electrolyte interphase for dendrite-free lithium metal anode, J. Colloid Interface Sci. 599 (2021) 819–827.
[5] P. Zou, Y. Wang, S.W. Chiang, X. Wang, F. Kang, C. Yang, Directing lateral growth of lithium dendrites in micro-compartmented anode arrays for safe lithium metal batteries, Nat. Commun. 9 (2018) 464.
[6] D. Lin, Y. Liu, Z. Liang, H.-W. Lee, J. Sun, H. Wang, K. Yan, J. Xie, Y.i. Cui, Layered reduced graphene oxide with nanoscale interlayer gaps as a stable host for lithium metal anodes, Nat. Nanotech. 11 (7) (2016) 626–632.
[7] Y.Y. Chen, G.Y. Zhou, W. Zong, Y. Ouyang, K. Chen, Y. Lv, Y.E. Miao, T.X. Liu, Porous polymer composite separators with three-dimensional ion-selective nanochannels for high-performance Li–S batteries, Compos. Commun. 25 (2021) 100679.
[8] C.Y. Zhou, W. Zong, G.Y. Zhou, X.S. Fan, Y.E. Miao, Radical-functionalized polymer nanofiber composite separator for ultra-stable dendritic-free lithium metal batteries, Compos. Commun. 25 (2021) 100696.
[9] Z. Dong, J. Wei, H. Yue, K. Zhang, L. Wang, X. Li, Z. Zhang, W. Yang, S. Yang, Multifunctional organosilicon compound contributes to stable operation of high-voltage lithium metal batteries, J. Colloid Interface Sci. 595 (2021) 35–42.
[10] H. Chen, A. Pei, D. Lin, J. Xie, A. Yang, J. Xu, K. Lin, J. Wang, H. Wang, F. Shi, D. Boyle, Y. Cui, Uniform high ionic conducting lithium sulfide protection layer for stable lithium metal anode, Adv. Energy Mater. 9 (2019) 1900858.
[11] C. Cao, Y.u. Li, Y. Feng, C. Peng, Z. Li, W. Feng, A solid-state single-ion polymer electrolyte with ultrahigh ionic conductivity for dendrite-free lithium metal batteries, Energy Storage Mater. 19 (2019) 401–407.
[12] C. Yan, X.B. Cheng, Y.X. Yao, X. Shen, B.Q. Li, W.J. Li, R. Zhang, J.Q. Huang, H. Li, Q. Zhang, An armored mixed conductor interphase on a dendrite-free lithium-metal anode, Adv. Mater. 30 (2018) 1804461.
[13] D. Lin, Y. Liu, W. Chen, G. Zhou, K. Liu, B. Dunn, Y.i. Cui, Conformal lithium fluoride protection layer on three-dimensional lithium by nonhazardous gaseous reagent freon, Nano Lett. 17 (6) (2017) 3731–3737.
[14] K. Lin, X. Qin, M. Liu, X. Xu, G. Liang, J. Wu, F. Kang, G. Chen, B. Li, Ultrafine titanium nitride sheath decorated carbon nanofiber network enabling stable lithium metal anodes, Adv. Funct. Mater. 29 (2019) 1903229.
[15] Z. Li, W. Ji, T.-X. Wang, Y. Zhang, Z. Li, X. Ding, B.-H. Han, W. Feng, Guiding uniformly distributed Li ion flux by lithiophilic covalent organic framework interlayers for high-performance lithium metal anodes, ACS Appl. Mater. Interfaces 13 (19) (2021) 22586–22596.
[16] Z. Ni, Y. Zhang, B. Zhu, Y. Wang, Y. Wang, X. Li, Y. Zhang, S. Sun, A multifunctional Cu6Sn5 interface layer for dendritic-free lithium metal anode, J. Colloid Interface Sci. 605 (2022) 223–230.
[17] M. Ishikawa, M. Morita, Y. Matsuda, In situ scanning vibrating electrode technique for lithium metal anodes, J. Power Sources 68 (2) (1997) 501–505.

[18] F. Ding, W.u. Xu, G.L. Graff, J. Zhang, M.L. Sushko, X. Chen, Y. Shao, M.H. Engelhard, Z. Nie, J. Xiao, X. Liu, P.V. Sushko, J. Liu, J.-G. Zhang, Dendrite-free lithium deposition via self-healing electrostatic shield mechanism, J. Am. Chem. Soc. 135 (11) (2013) 4450–4456.
[19] K. Yan, Z. Lu, H.W. Lee, F. Xiong, P.C. Hsu, Y. Li, J. Zhao, S. Chu, Y. Cui, Selective deposition and stable encapsulation of lithium through heterogeneous seeded growth, Nat. Energy 1 (2016) 16010.
[20] Q. Zhao, X. Hao, S. Su, J. Ma, Y.i. Hu, Y. Liu, F. Kang, Y.-B. He, Expanded-graphite embedded in lithium metal as dendrite-free anode of lithium metal batteries, J. Mater. Chem. A 7 (26) (2019) 15871–15879.
[21] M. Wan, S. Kang, L. Wang, H.W. Lee, G.W. Zheng, Y. Cui, Y. Sun, Mechanical rolling formation of interpenetrated lithium metal/lithium tin alloy foil for ultrahigh-rate battery anode, Nat. Commun. 11 (2020) 829.
[22] C.P. Yang, Y.X. Yin, S.F. Zhang, N.W. Li, Y.G. Guo, Accommodating lithium into 3D current collectors with a submicron skeleton towards long-life lithium metal anodes, Nat. Commun. 6 (2015) 8058.
[23] L. Pan, Z. Luo, Y. Zhang, W. Chen, Z. Zhao, Y. Li, J. Wan, D. Yu, H. He, D. Wang, Seed-free selective deposition of lithium metal into tough graphene framework for stable lithium metal anode, ACS Appl. Mater. Interfaces 11 (47) (2019) 44383–44389.
[24] X.-Y. Yue, W.-W. Wang, Q.-C. Wang, J.-K. Meng, Z.-Q. Zhang, X.-J. Wu, X.-Q. Yang, Y.-N. Zhou, CoO nanofiber decorated nickel foams as lithium dendrite suppressing host skeletons for high energy lithium metal batteries, Energy Storage Mater. 14 (2018) 335–344.
[25] S.H. Wang, Y.X. Yin, T.T. Zuo, W. Dong, J.Y. Li, J.L. Shi, C.H. Zhang, N.W. Li, C.J. Li, Y.G. Guo, Stable Li metal anodes via regulating lithium plating/stripping in vertically aligned microchannels, Adv. Mater. 29 (2017) 1703729.
[26] X. Shen, X. Cheng, P. Shi, J. Huang, X. Zhang, C. Yan, T. Li, Q. Zhang, Lithium–matrix composite anode protected by a solid electrolyte layer for stable lithium metal batteries, J. Energy Chem. 37 (2019) 29–34.
[27] T.T. Zuo, X.W. Wu, C.P. Yang, Y.X. Yin, H. Ye, N.W. Li, Y. g., Guo Graphitized carbon fibers as multifunctional 3D current collectors for high areal capacity li anodes, Adv. Mater. 29 (2017) 1700389.
[28] H. Jo, D. Song, Y.-C. Jeong, Y.M. Lee, M.-H. Ryou, Study on Dead-Li suppression mechanism of Li-hosting vapor-grown-carbon-nanofiber-based protective layer for Li metal anodes, J. Power Sources 409 (2019) 132–138.
[29] Y. Fang, Y. Zeng, Q.i. Jin, X.F. Lu, D. Luan, X. Zhang, X.W.(. Lou, Nitrogen-Doped Amorphous Zn–carbon multichannel fibers for stable lithium metal anodes, Angew. Chem. Int. Ed. 60 (15) (2021) 8515–8520.
[30] M. Lei, J.-G. Wang, L. Ren, D. Nan, C. Shen, K. Xie, X. Liu, Highly lithiophilic cobalt nitride nanobrush as a stable host for high-performance lithium metal anodes, ACS Appl. Mater. Interfaces 11 (34) (2019) 30992–30998.
[31] R. Zhang, X. Chen, X. Shen, X.-Q. Zhang, X.-R. Chen, X.-B. Cheng, C. Yan, C.-Z. Zhao, Q. Zhang, Coralloid carbon fiber-based composite lithium anode for robust lithium metal batteries, Joule 2 (4) (2018) 764–777.
[32] Z. Liang, D. Lin, J. Zhao, Z. Lu, Y. Liu, C. Liu, Y. Lu, H. Wang, K. Yan, X. Tao, Y.i. Cui, Composite lithium metal anode by melt infusion of lithium into a 3D conducting scaffold with lithiophilic coating, Proc. Natl. Acad. Sci. U.S.A. 113 (11) (2016) 2862–2867.
[33] T. Le, Q. Liang, M. Chen, C. Yang, Z. Yu, J. Cheng, F. Kang, Y. Yang, A triple-gradient host for long cycling lithium metal anodes at ultrahigh current density, Small 16 (2020) 2001992.
[34] X. Wang, L. Ma, Q. Ji, J.Q. Meng, S. Liang, Z. Xu, M. Wang, X. Zuo, Y. Xiao, J. Zhu, Y. Xia, P.M. Buschbaum, Y.J. Cheng, MnO/Metal/Carbon nanohybrid lithium-ion battery anode with enhanced electrochemical performance: universal facile scalable synthesis and fundamental understanding, Adv. Mater. Interfaces 6 (2019) 1900335.
[35] X. Wang, Z. Pan, Y. Wu, X. Ding, X. Hong, G. Xu, M. Liu, Y. Zhang, W. Li, Infiltrating lithium into carbon cloth decorated with zinc oxide arrays for dendrite-free lithium metal anode, Nano Res. 12 (3) (2019) 525–529.
[36] P. Xue, C. Sun, H. Li, J. Liang, C. Lai, Superlithiophilic Amorphous SiO_2 –TiO_2 distributed into porous carbon skeleton enabling uniform lithium deposition for stable lithium metal batteries, Adv. Sci. 6 (2019) 1900943.
[37] E. Peled, The Electrochemical behavior of alkali and alkaline earth metals in nonaqueous battery systems–the solid electrolyte interphase model, J. Electrochem. Soc. 126 (12) (1979) 2047–2051.
[38] X.-B. Cheng, R. Zhang, C.-Z. Zhao, Q. Zhang, Toward safe lithium metal anode in rechargeable batteries: A review, Chem. Rev. 117 (15) (2017) 10403–10473.
[39] X. Guan, A. Wang, S. Liu, G. Li, F. Liang, Y.W. Yang, X. Liu, J. Luo, Controlling nucleation in lithium metal anodes, Small 14 (2018) 1801423.
[40] P. Zou, S.W. Chiang, J. Li, Y. Wang, X. Wang, D. Wu, A. Nairan, F. Kang, C. Yang, Ni@Li_2O Co-axial nanowire based reticular anode: tuning electric field distribution for homogeneous lithium deposition, Energy Storage Mater. 18 (2019) 155–164.
[41] Q. Ma, X. Sun, P. Liu, Y. Xia, X. Liu, J. Luo, Bio-Inspired stable lithium-metal anodes by co-depositing lithium with a 2D vermiculite shuttle, Angew. Chem. Int. Ed. 58 (19) (2019) 6200–6206.
[42] L. Zhang, X. Yin, S. Shen, Y. Liu, T. Li, H. Wang, X. Lv, X. Qin, S.W. Chiang, Y. Fu, F. Kang, B. Li, Simultaneously homogenized electric field and ionic flux for reversible ultrahigh-areal-capacity li deposition, Nano Lett. 20 (8) (2020) 5662–5669.
[43] H. Saadi, F.I.H. Rhouma, Z. Benzarti, Z. Bougrioua, S. Guermazi, K. Khirouni, Electrical conductivity improvement of Fe doped ZnO nanopowders, Mater. Res. Bull. 129 (2020) 110884.
[44] R. Zhang, L. Fan, Y. Fang, S. Yang, Electrochemical route to the preparation of highly dispersed composites of ZnO/Carbon nanotubes with significantly enhanced electrochemiluminescence from ZnO, J. Mater. Chem. 18 (2008) 4964.
[45] R. Wahab, S.G. Ansari, Y.S. Kim, H.K. Seo, G.S. Kim, G. Khang, H.-S. Shin, low temperature solution synthesis and characterization of ZnO nano-flowers, Mater. Res. Bull. 42 (9) (2007) 1640–1648.
[46] C.H. Kim, B.-H. Kim, Zinc oxide/activated carbon nanofiber composites for high-performance supercapacitor electrodes, J. Power Sources 274 (2015) 512–520.
[47] N. Ibris, A.M. Salvi, M. Liberatore, F. Decker, A. Surca, XPS study of the li intercalation process in sol-gel-produced V_2O_5 thin film: Influence of substrate and film synthesis modification, Surf. Interface Anal. 37 (2005) 1092–1104.
[48] V. Perumal, U. Hashim, S.C.B. Gopinath, R. Haarindraprasad, K.L. Foo, S.R. Balakrishnan, P. Poopalan, 'Spotted Nanoflowers': Gold-seeded zinc oxide nanohybrid for selective bio-capture, Sci. Rep. 5 (2015) 12231.
[49] J. Liu, T. Xu, X. Sun, J. Bai, C. Li, Preparation of stable composite porous nanofibers carried SnOx-ZnO as a flexible supercapacitor material with excellent electrochemical and cycling performance, J. Alloys Compd. 807 (2019) 151652.
[50] G. Wang, X. Xiong, D. Xie, X. Fu, X. Ma, Y. Li, Y. Liu, Z. Lin, C. Yang, M. Liu, Suppressing dendrite growth by a functional electrolyte additive for robust Li metal anodes, Energy Storage Mater. 23 (2019) 701–706.
[51] C. Zhang, Q. Lan, Y. Liu, J. Wu, H. Shao, H. Zhan, Y. Yang, A dual-layered artificial solid electrolyte interphase formed by controlled electrochemical reduction of LiTFSI/DME-$LiNO_3$ for dendrite-free lithium metal anode, Electrochim. Acta 306 (2019) 407–419.
[52] S.-J. Zhang, J.-H. You, J.-D. Chen, Y.-Y. Hu, C.-W. Wang, Q. Liu, Y.-Y. Li, Y. Zhou, J.-T. Li, J. Świątowska, L. Huang, S.-G. Sun, Aluminum-based metal–organic frameworks derived Al_2O_3-loading mesoporous carbon as a host matrix for lithium-metal anodes, Adv. Mater. Interfaces 11 (51) (2019) 47939–47947.
[53] X. Wang, J. Zhuang, M. Liu, C. Wang, Y. Zhong, H. Wang, X. Cheng, S.i. Liu, G. Cao, W. Li, Facile and scalable engineering of a heterogeneous microstructure for uniform, stable and fast lithium plating/stripping, J. Mater. Chem. A. 7 (32) (2019) 19104–19111.
[54] S. Li, Y. Huang, W. Ren, X. Li, M. Wang, H. Cao, Stabilize lithium metal anode through in-situ forming a multi-component composite protective layer, Chem. Eng. J. 422 (2021) 129911.